OGLE-2011-BLG-0265Lb: A JOVIAN MICROLENSING PLANET ORBITING AN M DWARF

J. Skowron[1,67], I.-G. Shin[2], A. Udalski[1,67], C. Han[2,68,67], T. Sumi[3,69], Y. Shvartzvald[4,70], A. Gould[5,68],
D. Dominis Prester[6,71], R. A. Street[7,72], U. G. Jørgensen[8,9,73], D. P. Bennett[10,69], V. Bozza[11,12,73], M. K. Szymański[1],
M. Kubiak[1], G. Pietrzyński[1,13], I. Soszyński[1], R. Poleski[1,5], S. Kozłowski[1], P. Pietrukowicz[1], K. Ulaczyk[1],
Ł. Wyrzykowski[14,1]
(The OGLE Collaboration),
F. Abe[15], A. Bhattacharya[10], I. A. Bond[16], C. S. Botzler[17], M. Freeman[17], A. Fukui[18], D. Fukunaga[15], Y. Itow[15],
C. H. Ling[16], N. Koshimoto[3], K. Masuda[15], Y. Matsubara[15], Y. Muraki[19], S. Namba[3], K. Ohnishi[20], L. C. Philpott[21],
N. Rattenbury[17], T. Saito[22], D. J. Sullivan[23], D. Suzuki[3], P. J. Tristram[23], P. C. M. Yock[17]
(The MOA Collaboration),
D. Maoz[4], S. Kaspi[4], M. Friedmann[4]
(Wise group),
L. A. Almeida[24], V. Batista[5], G. Christie[25], J.-Y. Choi[2], D. L. DePoy[26], B. S. Gaudi[5], C. Henderson[5], K.-H. Hwang[2],
F. Jablonski[24], Y. K. Jung[2], C.-U. Lee[27], J. McCormick[28], T. Natusch[25,29], H. Ngan[25], H. Park[2], R. W. Pogge[5], J. C. Yee[5,30]
(The μFUN Collaboration),
M. D. Albrow[31], E. Bachelet[32], J.-P. Beaulieu[33], S. Brillant[34], J. A. R. Caldwell[35], A. Cassan[33], A. Cole[36],
E. Corrales[33], Ch. Coutures[33], S. Dieters[32], J. Donatowicz[37], P. Fouqué[32,38], J. Greenhill[36,68], N. Kains[39,40,72,73],
S. R. Kane[41], D. Kubas[33,34], J.-B. Marquette[33], R. Martin[42], J. Menzies[43], K. R. Pollard[31], C. Ranc[33], K. C. Sahu[40,73],
J. Wambsganss[44,73], A. Williams[44], D. Wouters[33]
(The PLANET Collaboration),
Y. Tsapras[7,45,71], D. M. Bramich[46], K. Horne[47,71], M. Hundertmark[47,48,73], C. Snodgrass[49,73], I. A. Steele[50]
(The RoboNet Collaboration),
and
K. A. Alsubai[51], P. Browne[47,72], M. J. Burgdorf[52], S. Calchi Novati[41,11,53,69], P. Dodds[47], M. Dominik[47,72], S. Dreizler[48],
X.-S. Fang[54], C.-H. Gu[54], Hardis[8], K. Harpsøe[8,9], F. V. Hessman[48], T. C. Hinse[27,8,55], A. Hornstrup[56], J. Jessen-Hansen[57],
E. Kerins[56], C. Liebig[47], M. Lund[57], M. Lundkvist[57,58], L. Mancini[59], M. Mathiasen[8], M. T. Penny[56,5], S. Rahvar[60,61],
D. Ricci[62,63,64], G. Scarpetta[11,12,53], J. Skottfelt[8,9], J. Southworth[65], J. Surdej[62], J. Tregloan-Reed[66], O. Wertz[66]
(The MiNDSTEp consortium)

[1] Warsaw University Observatory, Al. Ujazdowskie 4, 00-478 Warszawa, Poland
[2] Department of Physics, Institute for Astrophysics, Chungbuk National University, 371-763 Cheongju, Korea
[3] Dept. of Earth and Space Science, Graduate School of Science, Osaka University, 1-1 Machikaneyama-cho, Toyonaka, 560-0043 Osaka, Japan
[4] School of Physics and Astronomy, Tel-Aviv University, Tel-Aviv 69978, Israel
[5] Department of Astronomy, Ohio State University, 140 West 18th Avenue, Columbus, OH 43210, USA
[6] Physics Department, Faculty of Arts and Sciences, University of Rijeka, Omladinska 14, 51000 Rijeka, Croatia
[7] Las Cumbres Observatory Global Telescope Network, 6740 Cortona Drive, suite 102, Goleta, CA 93117, USA
[8] Niels Bohr Institute, University of Copenhagen, Juliane Maries vej 30, 2100 Copenhagen, Denmark
[9] Centre for Star and Planet Formation, Geological Museum, Øster Voldgade 5, 1350 Copenhagen, Denmark
[10] Dept. of Physics, University of Notre Dame, Notre Dame, IN 46556, USA
[11] Dipartimento di Fisica "E.R. Caianiello" Università degli Studi di Salerno Via Giovanni Paolo II - I 84084 Fisciano (SA) - Italy
[12] Istituto Nazionale di Fisica Nucleare, Sezione di Napoli, Italy
[13] Universidad de Concepción, Departamento de Astronomia, Casilla 160-C, Concepción, Chile
[14] Institute of Astronomy, University of Cambridge, Madingley Road, Cambridge CB3 0HA, UK
[15] Solar-Terrestrial Environment Laboratory, Nagoya University, 464-8601 Nagoya, Japan
[16] Institute of Information and Mathematical Sciences, Massey University, Private Bag 102-904, North Shore Mail Centre, Auckland, New Zealand
[17] Dept. of Physics, University of Auckland, Private Bag 92019, Auckland, New Zealand
[18] Okayama Astrophysical Observatory, National Astronomical Observatory of Japan, Asakuchi, 719-0232 Okayama, Japan
[19] Dept. of Physics, Konan University, Nishiokamoto 8-9-1, 658-8501 Kobe, Japan
[20] Nagano National College of Technology, 381-8550 Nagano, Japan
[21] Department of Earth, Ocean and Atmospheric Sciences, University of British Columbia, Vancouver, British Columbia, V6T 1Z4, Canada
[22] Tokyo Metropolitan College of Industrial Technology, 116-8523 Tokyo, Japan
[23] School of Chemical and Physical Sciences, Victoria University, Wellington, New Zealand
[24] Divisão de Astrofisica, Instituto Nacional de Pesquisas Espeaciais, Avenida dos Astronauntas, 1758 Sao José dos Campos, 12227-010 SP, Brazil
[25] Auckland Observatory, 670 Manukau Rd, Royal Oak 1023, Auckland, New Zealand
[26] Dept. of Physics and Astronomy, Texas A&M University College Station, TX 77843-4242, USA
[27] Korea Astronomy and Space Science Institute, 305-348 Daejeon, Korea
[28] Farm Cove Observatory, Centre for Backyard Astrophysics, Pakuranga, Auckland, New Zealand
[29] Institute for Radiophysics and Space Research, AUT University, Auckland, New Zealand
[30] Harvard-Smithsonian Center for Astrophysics, 60 Garden St., Cambridge, MA 02138, USA
[31] University of Canterbury, Dept. of Physics and Astronomy, Private Bag 4800, 8020 Christchurch, New Zealand
[32] Université de Toulouse, UPS-OMP, IRAP, 31400 Toulouse, France
[33] UPMC-CNRS, UMR7095, Institut d'Astrophysique de Paris, 98bis boulevard Arago, 75014 Paris, France
[34] European Southern Observatory (ESO), Alonso de Cordova 3107, Casilla 19001, Santiago 19, Chile
[35] McDonald Observatory, 16120 St Hwy Spur 78 #2, Fort Davis, TX 79734, USA
[36] School of Math and Physics, University of Tasmania, Private Bag 37, GPO Hobart, 7001 Tasmania, Australia

[37] Technical University of Vienna, Department of Computing,Wiedner Hauptstrasse 10, Vienna, Austria
[38] CFHT Corporation, 65-1238 Mamalahoa Hwy, Kamuela, HI, 96743, USA
[39] European Southern Observatory, Karl-Schwarzschild-Str. 2, 85748 Garching bei München, Germany
[40] Space Telescope Science Institute, 3700 San Martin Drive, Baltimore, MD 21218, USA
[41] NASA Exoplanet Science Institute, Caltech, MS 100-22, 770 S. Wilson Ave., Pasadena, CA 91125, USA
[42] Perth Observatory, Walnut Road, Bickley, 6076 Perth, Australia
[43] South African Astronomical Observatory, PO Box 9, Observatory 7935, South Africa
[44] Astronomisches Rechen-Institut, Zentrum für Astronomie der Universität Heidelberg (ZAH), Mönchhofstr. 12-14, 69120 Heidelberg, Germany
[45] School of Physics and Astronomy, Queen Mary University of London, Mile End Road, London E1 4NS, UK
[46] Qatar Environment and Energy Research Institute, Qatar Foundation, P. O. Box 5825, Doha, Qatar
[47] SUPA School of Physics & Astronomy, University of St Andrews, North Haugh, St Andrews, KY16 9SS, UK
[48] Institut für Astrophysik, Georg-August-Universität, Friedrich-Hund-Platz 1, 37077 Göttingen, Germany
[49] Max Planck Institute for Solar System Research, Justus-von-Liebig-Weg 3, 37077 Göttingen, Germany
[50] Astrophysics Research Institute, Liverpool John Moores University, Liverpool CH41 1LD, UK
[51] Qatar Foundation, PO Box 5825, Doha, Qatar
[52] HE Space Operations GmbH, Flughafenallee 24, 28199 Bremen, Germany
[53] Istituto Internazionale per gli Alti Studi Scientifici (IIASS), Via Giuseppe Pellegrino, 19, 84019 Vietri Sul Mare Salerno, Italy
[54] National Astronomical Observatories / Yunnan Observatory, Key Laboratory for the Structure and Evolution of Celestial Objects, Chinese Academy of Sciences, Kunming 650011, China
[55] Armagh Observatory, College Hill, Armagh, BT61 9DG, Northern Ireland, UK
[56] Jodrell Bank Centre for Astrophysics, University of Manchester, Oxford Road, Manchester, M13 9PL, UK
[57] Department of Physics and Astronomy, Aarhus University, Ny Munkegade 120, Århus C, Denmark
[58] Stellar Astrophysics Centre, Department of Physics and Astronomy, Aarhus University, Ny Munkegade 120, DK-8000 Aarhus C, Denmark
[59] Max Planck Institute for Astronomy, Königstuhl 17, 69117 Heidelberg, Germany
[60] Department of Physics, Sharif University of Technology, PO Box 11155–9161, Tehran, Iran
[61] Perimeter Institute for Theoretical Physics, 31 Caroline St. N., Waterloo ON, N2L 2Y5, Canada
[62] Institut d'Astrophysique et de Géophysique, Allé du 6 Août 17, Sart Tilman, Bât. B5c, 4000 Liége, Belgium
[63] INAF/Istituto di Astrofisica Spaziale e Fisica Cosmica, Via Gobetti 101, Bologna, Italy
[64] Instituto de Astronomía, UNAM, AP 877, Ensenada, B.C. 22800, Mexico
[65] Astrophysics Group, Keele University, Staffordshire, ST5 5BG, UK
[66] NASA Ames Research Center, Moffett Field CA 94035, USA

ABSTRACT

We report the discovery of a Jupiter-mass planet orbiting an M-dwarf star that gave rise to the microlensing event OGLE-2011-BLG-0265. Such a system is very rare among known planetary systems and thus the discovery is important for theoretical studies of planetary formation and evolution. High-cadence temporal coverage of the planetary signal, combined with extended observations throughout the event, allows us to accurately model the observed light curve. However, the final microlensing solution remains degenerate, yielding two possible configurations of the planet and the host star. In the case of the preferred solution, the mass of the planet is $M_p = 0.9 \pm 0.3\ M_J$, and the planet is orbiting a star with a mass $M = 0.22 \pm 0.06\ M_\odot$. The second possible configuration (2σ away) consists of a planet with $M_p = 0.6 \pm 0.3\ M_J$ and host star with $M = 0.14 \pm 0.06\ M_\odot$. The system is located in the Galactic disk 3–4 kpc toward the Galactic bulge. In both cases, with an orbit size of 1.5–2.0 AU, the planet is a "cold Jupiter"—located well beyond the "snow line" of the host star. Currently available data make the secure selection of the correct solution difficult, but there are prospects for lifting the degeneracy with additional follow-up observations in the future, when the lens and source star separate.

Key words: gravitational lensing: micro – planetary systems

1. INTRODUCTION

In the recent decade, gravitational lensing has proven to be one of the major techniques of detecting and characterizing extrasolar planetary systems. Due to the favorable geometry in the Galaxy where microlensing phenomena occur, this technique is sensitive to planets orbiting their host stars with separations 0.5–10 AU. The technique is sensitive to low-mass planets—down to Earth-mass planets and even smaller masses if observed from space. It can also detect planets not bound to stars—free-floating planets (Sumi et al. 2011). Therefore, it provides an important tool that enables a census of extrasolar planets in a very important region of parameter space that is generally inaccessible to other techniques: the region beyond the snow line where cold giant planets are most probably forming. Such a census will be complementary to the one provided by transit and radial-velocity surveys.

First assessments of the planet frequency in the microlensing domain have already been published (Tsapras et al. 2003; Gould et al. 2010; Sumi et al. 2010; Cassan et al. 2012). However, these studies were based on a limited number of planetary microlensing events. Precise analysis requires a much larger number of microlensing planets. New observational strategies of microlensing experiments have been implemented

---

[66] Corresponding author.
[67] Deceased 2014 September 28.
[68] The MiNDSTEp Consortium.
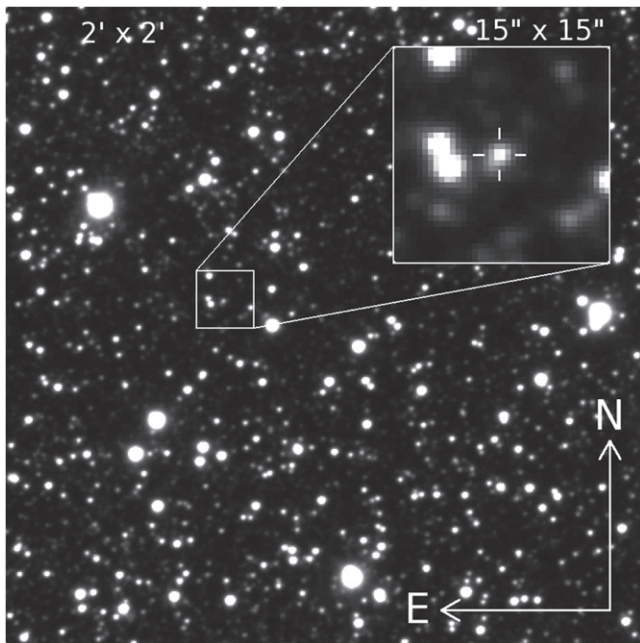[69] The OGLE Collaboration.
[70] The MOA Collaboration.
[71] The Wise Group.
[72] The μFUN Collaboration.
[73] The PLANET Collaboration.
[74] The RoboNet Collaboration.
[75] Sagan Visiting Fellow.

Figure 1. Finding chart for the microlensing event OGLE-2011-BLG-0265 as seen at the baseline level in 2010. The position of the source star (and the lens) is marked with the white cross, $(\alpha,\delta)_{J2000} = (17^{h}57^{m}47^{s}.72, -27°23'40''.3) \pm 0''.1$. The field of view is $2' \times 2'$, while the inset covers $15'' \times 15''$. Pixel scale is $0.26''$/pixel. North is up and east is to the left. The brightest stars in the inset are $I \sim 16.2 - 16.4$, while the faintest visible at this scale are $I \sim 20$. The brightest star in the whole chart is TYC 6849-852-1 ($I \approx 11$).

in the last several years, leading to significant increase of the number of planet detections.

After the initial period of pioneering detections, the planetary microlensing field has undergone rapid changes and continues to evolve toward the next-generation experiments. The traditional first-generation approach was that some selected microlensing events detected by large-scale surveys like the Optical Gravitational Lensing Experiment (OGLE) and the Microlensing Observation in Astrophysics (MOA) projects were densely observed by follow-up groups such as μFUN, PLANET, RoboNet, and MiNDSTEp. Since then, the experiments have adopted more sophisticated observing strategies. For example, the second-generation microlensing surveys consist of a network of wide-field telescopes that are capable of observing large areas of the Galactic bulge field with high cadences of about 10–20 minutes. Starting from the 2010 observing season when the fourth phase of the OGLE survey began regular observations with the 1.3 m telescope at the Las Campanas Observatory in Chile, the second-generation microlensing network began to take shape. The OGLE-IV observing setup, together with the 1.8 m MOA-II telescope located at Mount John Observatory in New Zealand and the 1 m telescope at the Wise Observatory in Israel, became the backbone of the second-generation network capable of conducting round-the-clock observations of selected fields in the Galactic bulge. There has also been progress in follow-up observations, including the formation of new-generation follow-up networks with enhanced observing capability (e.g., RoboNet, a network of robotic telescopes from LCOGT and the Liverpool Telescope).

One of the most important discoveries made with the microlensing technique is the detection of cold giant planets

orbiting faint M-type dwarf stars. These discoveries were possible because microlensing does not rely on the light from a host star in order to detect a planet. This implies that the dependency of the microlensing sensitivity to planets on the spectral type of host stars is weak and the sensitivity extends down to late M dwarfs and beyond.

Studying planets around M dwarfs is important because these stars comprise ~70–75% of stars in the Solar neighborhood and the Galaxy as a whole. Planets around M dwarfs have been probed by the radial-velocity and transit methods (e.g., Delfosse et al. 1998; Marcy et al. 1998; Charbonneau et al. 2009; Bonfils et al. 2011; Montet et al. 2014). However, the low luminosity of M dwarfs poses serious difficulties in searching for planets with these methods. Furthermore, the host stars of the M-dwarf planets discovered so far tend to occupy the brighter end of the M-dwarf range. As a result, the characteristics of the lower-mass M-dwarf planet population are essentially unknown. In addition, all M-dwarf planets detected by the radial-velocity method are located within only a few dozens of parsecs from the Sun, and thus the sample of these planets is greatly biased not only to the spectral type of host stars but also to the distance from the Solar system.

By contrast, the most frequent host stars of microlensing planets are M dwarfs, including a planet with its host star directly imaged (Bennett et al. 2008; Kubas et al. 2012) and several others whose masses are constrained by microlensing light curves and auxiliary data (Udalski et al. 2005; Beaulieu et al. 2006; Gaudi et al. 2008; Dong et al. 2009; Bennett et al. 2010; Batista et al. 2011; Kains et al. 2013; Street et al. 2013; Poleski et al. 2014; Shvartzvald et al. 2014; Tsapras et al. 2014). In addition, lensing events occur regardless of the stellar types of lensing objects and thus one can obtain a sample of planetary systems that is unbiased by the stellar types of host stars. Furthermore, lensing events occur by objects distributed in a wide range of the Galaxy between the Earth and the Galactic center, and thus one can obtain a planet sample that is more representative of the whole Galaxy.

Constructing an unbiased sample of planets around M dwarfs is important for understanding the formation mechanism of these planets. A theory based on the core accretion mechanism predicts that gas giants form much less frequently around M dwarfs than around Sun-like stars, while terrestrial and ice giant planets may be relatively common (Laughlin et al. 2004; Ida & Lin 2005). An alternative theory based on the disk instability mechanism predicts that giant planets can form around M dwarfs (Boss 2006), which contradicts the prediction of planet formation by the core accretion mechanism. Therefore, determining the characteristics and the frequency of the planets orbiting M dwarfs is important in order to refine the planetary formation scenario of these planets.

In this paper, we report the discovery of another giant planet orbiting an M3-M4 dwarf that was detected from the light curve analysis of the microlensing event OGLE-2011-BLG-0265. Although modeling the microlensing light curve yields two solutions that cannot be fully distinguished with the currently available data, both solutions indicate a Jupiter-mass planet. There is good prospect on resolving the ambiguity of the solutions in the future when the lens and the source separate.
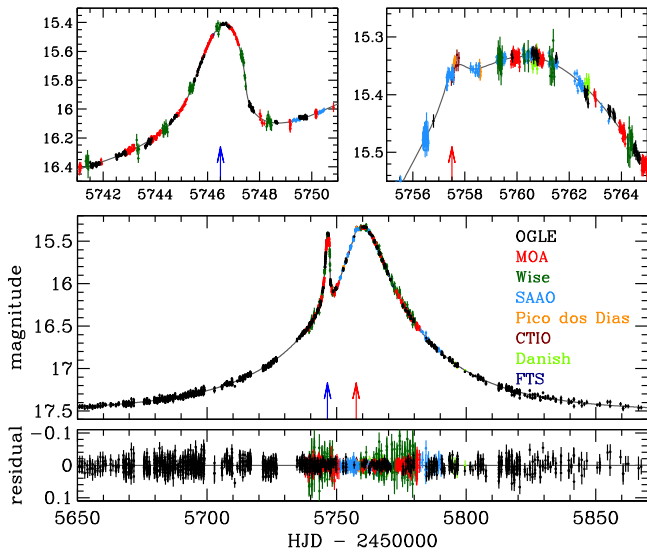
Figure 2. Light curve of the microlensing event OGLE-2011-BLG-0265. Only a subset of data taken during the event is presented—lower signal-to-noise observations, as well as, data providing little constraint on the final solution are omitted. The colors of the data points are chosen to match those of the labels of observatories. The solid curve superposed on the data points represents the best-fit model curve ($u_0 > 0$). The model curve for the $u_0 < 0$ solution would be visually indistinguishable. The two upper panels show the enlarged view of the major (HJD $\sim$ 2455746.5) and minor ($\sim$2455757.5) planetary perturbation regions (marked with arrows).

2. OBSERVATIONS AND DATA

The gravitational microlensing event OGLE-2011-BLG-0265 was discovered on 2011 April 16 by the OGLE Early Warning System during the test phase of its implementation for the OGLE-IV survey. It was officially announced on 2011 May 25 as one of 431 events in the inauguration set of events detected during the 2011 season. The event was also found by the MOA group and designated as MOA-2011-BLG-197.

The microlensed source star of the event is located at $(\alpha, \delta)_{J2000} = (17^h57^m47^s.72, -27°23'40''.3)$ in equatorial coordinates and $(l, b) = (2°.70, -1°.52)$ in Galactic coordinates (with the accuracy of the absolute position of the order of 0.1 arcsec). This region of the sky corresponds to the densest stellar region in the Galactic bulge toward which the vast majority of microlensing events are being detected. Figure 1 shows the finding chart of the event taken in 2010 when the source had not yet been magnified. The brightness and color of the event at the baseline, calibrated to the standard VI system, are $I = 17.51$ and $V - I = 3.03$, respectively.

The OGLE-IV survey is conducted using the 1.3 m Warsaw telescope equipped with the 32-CCD mosaic camera located at the Las Campanas Observatory in Chile. A single image covers approximately 1.4 square degrees with a resolution of 0.26 arcsec/pixel. OGLE-2011-BLG-0265 is located in the "BLG504" OGLE-IV field, which was observed with an 18 minute cadence in the 2011 season. See the OGLE Web page or the map of the sky coverage.[76] The exposure time was 100 s and the variability monitoring was performed in the I-band filter. Several V-band images were also taken during the event in order to determine the color of the source star. The analyzed OGLE-IV data set of the event contains 3749 epochs covering three observing seasons 2010–2012.

The MOA project is regularly surveying the Galactic bulge with the 1.8 m telescope at the Mt. John Observatory in New Zealand. Images are collected with a 10-CCD mosaic camera covering $\approx$2.2 square degrees. OGLE-2011-BLG-0265 lies in the high-cadence MOA field "gb10" that is typically visited a few times per hour, enabling it to take 4774 epochs in total during the 2006–2012 seasons. Observations were conducted using the wide non-standard R/I filter with the exposure time of 60 s.

OGLE-2011-BLG-0265 is also located in the footprint of the survey conducted at the Wise Observatory in Israel with the 1.0 m telescope and four-CCD mosaic camera, LAIWO (Shvartzvald & Maoz 2012). This site fills the longitudinal gap between the OGLE and MOA sites, enabling round-the-clock coverage of the event. In total 710 epochs were obtained from this survey. Observations were carried out with the I-band filter and the exposure time was 180 s.

The OGLE-2011-BLG-0265 event turned out to evolve relatively slowly. Data collected by survey observations have good enough coverage of the anomaly and overall light curve to identify the planetary nature of the event. Nevertheless, the phenomenon was also monitored by several follow-up groups based on the anomaly alert issued on 2011 July 2 by the MOA group. It should be noted that the OGLE group generally does not issue alerts of ongoing anomalies in the present phase.

The groups that participated in the follow-up observations include the Probing Lensing Anomalies NETwork (PLANET: Beaulieu et al. 2006), Microlensing Follow-up Network (μFUN: Gould et al. 2006), RoboNet (Tsapras et al. 2009), and MiNDSTEp (Dominik et al. 2010). The telescopes used for these observations include PLANET 1.0 m of South African Astronomical Observatory (SAAO) in South Africa, PLANET 0.6 m of Perth Observatory in Australia, μFUN 1.3 m SMARTS telescope of Cerro Tololo Inter-American Observatory (CTIO) in Chile, μFUN 0.4 m of Auckland Observatory in New Zealand, μFUN 0.36 m of Farm Cove Observatory (FCO) in New Zealand, μFUN 0.8 m of Observatorio del Teide in Tenerife, Spain, μFUN 0.6 m of Observatorio do Pico dos Dias (OPD) in Brazil, μFUN 0.4 m of Marty S. Kraar Observatory of Weizmann Institute of Science (Weizmann) in Israel, MiNDSTEp Danish 1.54 m telescope at La Silla Observatory in Chile, 2.0 m Liverpool Telescope at La Palma, RoboNet FTN 2.0 m in Hawaii, and RoboNet FTS 2.0 m in Australia.

By the time the first anomaly had ended, a series of solutions of lensing parameters based on independent real-time modeling were released. A consistent interpretation of these analyses was that the anomaly was produced by a planetary companion to the lens star. The models also predicted that there would be another perturbation about 10 days after the first anomaly, followed by the event peak just after the second anomaly. Based on this prediction, follow-up observations were continued beyond the main anomaly, up to the peak and even beyond. This enabled dense coverage of the second anomaly, which turned out to be important for the precise characterization of the lens system. See Section 4.1.

The event did not return to its baseline until the end of the 2011 season—HJD′ (=HJD − 2450000) $\sim$ 5870. In order to obtain baseline data, observations were resumed in the 2012 season, which started on HJD′ $\sim$ 5960. Combined survey and follow-up photometry constitute a very continuous and complete data set with the very dense coverage of the planetary anomaly.

Data acquired from different observatories were reduced using photometry codes developed by the individual groups. The photometry codes used by the OGLE and MOA groups, developed respectively by Udalski (2003) and Bond et al. (2001), were based on the Difference Image Analysis method (Alard & Lupton 1998). The PySIS pipeline (Albrow et al. 2009) was used for the reduction of the PLANET data and the Wise data. The μFUN data were processed using the DoPHOT pipeline (Schechter et al. 1993). For the RoboNet and MiNDSTEp data, the DanDIA pipeline (Bramich 2008) was used.

To analyze the data sets obtained from different observatories, we rescale the reported uncertainties for each data set (see Skowron et al. 2011). The microlensing magnification significantly changes the brightness of the measured object during the event, and it is often the case that the reported uncertainties by the automatic pipelines are underestimated by different amounts. To account for this, we first adjust uncertainties by introducing a quadratic term so that the cumulative distribution function of χ^2 as a function of magnification becomes linear. We then rescale the error bars so that χ^2 per degree of freedom (dof) becomes unity for each data set, where the value of χ^2 is derived from the best-fit solution. This process greatly helps to estimate uncertainties of the lensing parameters. It is done in an iterative manner using the full model (i.e., with the effects of the parallax and orbital motion taken into account).

Figure 2 shows the light curve of OGLE-2011-BLG-0265. The subset of the gathered data that were used in the final calculations are presented. For the most part, the light curve is well represented by a smooth and symmetric curve of a standard lensing event caused by a single-mass object (Paczyński 1986) except for the short-term perturbations at HJD′ ∼ 5746.5 (major perturbation) and 5757.5 (minor perturbation), which lasted for ∼4 days and ∼1 day, respectively. These short-term perturbations are characteristic features of planetary microlensing (Mao & Paczyński 1991; Gould & Loeb 1992).

The dense temporal coverage from the multiple sites is useful in ensuring that there is no missing feature in the light curve. Also, overlapping observations allow to perform extensive self consistency checks among the data sets. After investigating residuals of all data sets used in the initial fits and correlating them with the observing conditions at the sites (seeing, sky background, and airmass), we carefully remove points for which we are less confident. Also, we do not use data sets that add no or little constraint to the light curve—such as data taken during only two or three nights of observations, or data taken during the monotonic decline of the event after planetary anomalies. The procedure of keeping smaller numbers of confident data points allows us to limit the influence of potential systematic errors and increase our confidence in the results, while, due to the redundancy of the gathered data, not harming the discriminatory power of the light curve.

3. MODELING THE LIGHT CURVE

Planetary lensing is a special case of the binary lensing where the mass ratio between the lens components is very small. The description of a binary-lensing light curve requires seven basic parameters. The first three parameters characterize the geometry of the lens-source approach, including the timescale for the source to cross the radius of the Einstein ring, $t_{\rm E}$ (Einstein timescale), the time of the closest source approach to a reference position of the lens system, t_0, and the lens-source separation at t_0, u_0 (impact parameter). For the reference position of the lens, we use the center of mass of the binary system. The Einstein ring denotes the image of a source for the case of the exact lens-source alignment. Its angular radius, $\theta_{\rm E}$ (Einstein radius), is commonly used as a length scale in describing the lensing phenomenon and the lens-source impact parameter u_0 is normalized to $\theta_{\rm E}$. Another three parameters needed to characterize the binary lens include the mass ratio between the lens components, q, the projected binary separation in units of the Einstein radius, s, and the angle of the binary axis in respect to the lens-source relative motion, α. The last parameter is the angular source radius θ_* normalized to $\theta_{\rm E}$ (i.e., $\rho = \theta_*/\theta_{\rm E}$; normalized source radius). This parameter is needed to describe the planet-induced perturbation during which the light curve is affected by the finite size of a source star (Bennett & Rhie 1996).

In addition to the basic binary-lensing parameters, several higher-order parameters are often needed to describe the subtle light curve deviations. OGLE-2011-BLG-0265 lasted nearly throughout the whole bulge season. For such a long timescale event, the motion of the source with respect to the lens may deviate from a rectilinear motion due to the change of the observer's position caused by the Earth's orbital motion around the Sun, and this can cause a long-term deviation in the light curve (Gould 1992). Consideration of this so-called "parallax" effect in modeling a microlensing light curve requires us to include two additional parameters of $\pi_{{\rm E},N}$ and $\pi_{{\rm E},E}$, which represent the two components of the lens parallax vector $\pi_{\rm E}$ projected on the sky in the north and east equatorial coordinates, respectively. The direction of the parallax vector corresponds to the relative lens-source motion in the frame of the earth at a specific time ($t_{0,\rm par}$). We use $t_{0,\rm par} = 2455760.1$. The size of the parallax vector is related to the Einstein radius $\theta_{\rm E}$ and the relative lens-source parallax $\pi_{\rm rel} = {\rm AU}(D_{\rm L}^{-1} - D_{\rm S}^{-1})$ by

$$\pi_{\rm E} = \frac{\pi_{\rm rel}}{\theta_{\rm E}}, \qquad (1)$$

where $D_{\rm L}$ and $D_{\rm S}$ are the distances to the lens and source, respectively. Measurement of the lens parallax is important because it, along with the Einstein radius, allows one to determine the lens mass and distance to the lens as

$$M = \frac{\theta_{\rm E}}{\kappa \pi_{\rm E}} \qquad (2)$$

and

$$D_{\rm L} = \frac{\rm AU}{\pi_{\rm E}\theta_{\rm E} + \pi_{\rm S}}, \qquad (3)$$

respectively (Gould 1992). Here $\kappa = 4\,G/(c^2{\rm AU})$ and $\pi_{\rm S} = {\rm AU}/D_{\rm S}$ represents the parallax of the source star.

Another effect that often needs to be considered in modeling long timescale lensing events is the orbital motion of the lens (Albrow et al. 2000; Penny et al. 2011; Shin et al. 2011; Park et al. 2013). The lens orbital motion affects the light curve by causing both the projected binary separation s and the binary axis angle α to change in time. It is especially important for the binary-lensing systems whose separation on the sky is close to

Table 1
Lensing Parameters

Parameter	$u_0 > 0$ Solution	$u_0 < 0$ Solution
χ^2/dof	4381.0/4470	4386.7/4470
t_0 (HJD$'$)	5760.0949 ± 0.0086	5760.0925 ± 0.0085
$t_{\rm eff}$ (days)	6.955 ± 0.017	-6.843 ± 0.031
$t_{\rm E}$ (days)	53.63 ± 0.19	53.33 ± 0.27
t_* (days)	0.5248 ± 0.0055	0.5173 ± 0.0053
q (10^{-3})	3.954 ± 0.063	3.923 ± 0.059
s_0	1.03900 ± 0.00086	1.03790 ± 0.00085
α_0 (deg)	-27.15 ± 0.14	25.96 ± 0.23
$\pi_{\rm E,N}$	0.238 ± 0.060	0.38 ± 0.11
$\pi_{\rm E,E}$	0.042 ± 0.017	0.061 ± 0.016
ds/dt (yr^{-1})	0.354 ± 0.019	0.369 ± 0.019
$d\alpha/dt$ (deg yr^{-1})	52.9 ± 6.3	-24.2 ± 7.7
$F_{\rm S,OGLE}$	1.860 ± 0.010	1.8380 ± 0.0096
$F_{\rm base,OGLE}$	1.92436 ± 0.00091	1.92519 ± 0.00087

Note. HJD$'$ = HJD − 2450000. α_0 and s_0 denote the projected binary axis angle and separation for the epoch $t_{\rm 0,orb} = 2455748.0$, respectively. The reference position for the definition of t_0 and u_0 is set as the center of mass of the lens system, $t_{\rm eff} = u_0 \cdot t_{\rm E}$. The geocentric reference frame is set in respect to the Earth velocity at $t_{\rm 0,par} = 2455760.1$. The flux unit for $F_{\rm S}$ and $F_{\rm base}$ is 18 mag for the instrumental and ∼18.22 for the calibrated OGLE I-band data. (See Figure 3 for the lens geometry and Figure 5 for the CMD.)

their Einstein ring radius (as we experience in this event). The shape of the emerging "resonant caustic" is very sensitive to the change of the binary separation. Also, such a caustic is considerably larger than the caustics produced by other lens configurations, allowing a larger part of the lens plane to be accurately probed during the event. We account for the orbital effect by assuming that the change rates of the projected binary separation, ds/dt, and the angular speed, $d\alpha/dt$, are constant. This is a sufficient approximation, as we expect the orbital periods to be significantly larger than the 11 day period between the perturbations seen in the light curve.

Since the binary separation is now a function of time, we quote the tables and use as fit parameters the value of the binary separation (s_0) and the binary axis angle (α_0) for a specific epoch: $t_{\rm 0,orb}$. Here, we choose to be 2455748.0.[77] We closely follow the conventions of the lensing parameters described in Skowron et al. (2011) with one difference; since we use α as an angle of the binary axis with respect to the lens-source trajectory, $d\alpha/dt$ describes the rotation of the binary axis in the plane of the sky.

The deviation in a lensing light curve caused by the orbital effect can be smooth and similar to the deviation induced by the parallax effect. Therefore, considering the orbital effect is important because it might affect the lens parallax measurement and thus the physical parameters of the lens (Batista et al. 2011; Skowron et al. 2011).

With the lensing parameters, we test different models of the light curve. In the first model (the standard model), the light curve is fitted with use of the seven basic lensing parameters. In the second model (the parallax model), we additionally consider the parallax effect by adding two parallax parameters: $\pi_{\rm E,N}$ and $\pi_{\rm E,E}$. In the third model (the orbit model), we consider

only the orbital motion of the lens by including the orbital parameters ds/dt and $d\alpha/dt$, but do not consider the parallax effect. In the last model (the parallax+orbit model), we include both: the orbital motion of the lens and the orbital motion of the Earth (which gives rise to the parallax effect).

For a basic binary model, every source trajectory has its exact mirror counterpart with respect to the star-planet axis—with $(u_0, \alpha) \rightarrow -(u_0, \alpha)$ being the only difference. However, when the additional effects are considered, each of the two trajectories with $u_0 > 0$ and $u_0 < 0$ deviate from a straight line and the pair of trajectories are no longer symmetric. The models with $u_0 > 0$ and $u_0 < 0$ can be degenerate, especially for events associated with source stars located near the ecliptic plane—this is known as the "ecliptic degeneracy" (Skowron et al. 2011). For OGLE-2011-BLG-0265, the source star is located at $\beta \sim 2°.7$ and thus we check both $u_0 > 0$ and $u_0 < 0$ solutions.

In modeling the OGLE-2011-BLG-0265 light curve, we search for the set of lensing parameters that best describes the observed light curve by minimizing χ^2 in the parameter space. We conduct this search through three steps. In the first step, grid searches are conducted over the space of a set of parameters, while the remaining parameters are searched by using a downhill approach (Dong et al. 2006). We then identify local minima in the grid-parameter space by inspecting the χ^2 distribution. In the second step, we investigate the individual local minima found from the initial search and refine the individual local solutions. In the final step, we choose a global solution by comparing the χ^2 values of the individual local minima. This multi-step procedure is needed to probe the existence of any possible degenerate solutions. We choose s, q, and α as the grid parameters because they are related to the light curve features in a complex way, such that a small change in their values can lead to dramatic changes in lensing light curves. On the other hand, the light curve shape depends smoothly on the remaining parameters, and thus they are searched for by using a downhill approach. For the χ^2 minimization for refinement and characterization of the solutions, we use the Markov Chain Monte Carlo (MCMC) method.

A planetary perturbation is mostly produced by the approach of the source star close to caustics that represent the positions on the source plane at which the lensing magnification of a point source becomes infinite. During the approach, lensing magnifications are affected by finite-source effects due to the differential magnification caused by the steep gradient of the magnification pattern around the caustic. For the computation of finite-source magnifications, we use the ray-shooting method (Schneider & Weiss 1986; Kayser et al. 1986; Wambsganss 1997). In this method, a large number of rays are uniformly shot from the image plane, which is bent according to the lens equation, and land on the source plane. The lens equation for image mapping from the image plane to the source plane is expressed as

$$\zeta = z - \frac{1}{1+q} \left(\frac{1}{\bar{z} - \bar{z}_{\rm L,1}} + \frac{q}{\bar{z} - \bar{z}_{\rm L,2}} \right), \qquad (4)$$

where ζ, $z_{\rm L}$, and z are the complex notations of the source, lens, and image positions, respectively, and the overbar denotes complex conjugate. Here all lengths are expressed in units of the Einstein radius. The finite magnification is computed as the

---

[77] Depending on the geometry of the event, different values of $t_{\rm 0,orb}$ yield different correlations between the parameters describing the event, hence, $t_{\rm 0,orb}$ equal to $t_{\rm 0,par}$ is not always the best choice in modeling.
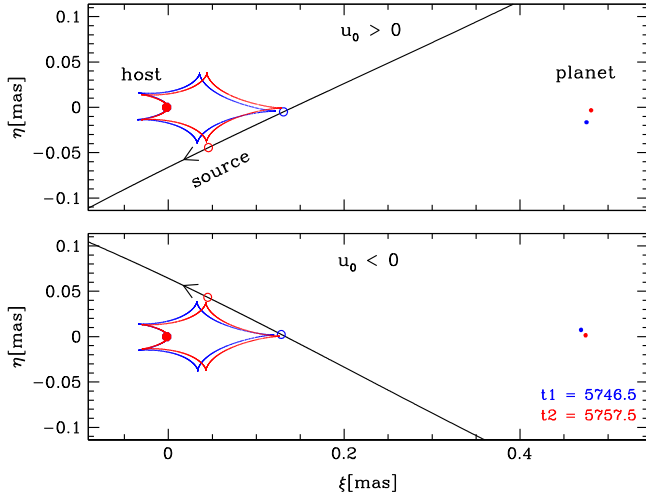
Figure 3. Geometry of the lensing system and the source star trajectory projected onto the plane of the sky. The upper panel is for the best-fit solution with $u_0 > 0$ and the lower panel is for the $u_0 < 0$ solution. The $u_0 > 0$ solution provides a slightly better fit than the $u_0 < 0$ solution by $\Delta\chi^2 = 5.7$. The closed figures with cusps represent the caustics at two different epochs, $HJD' = 5746.5$ and 5757.5, which correspond to the moments of the major and minor perturbation in the light curve. The line with an arrow represents the source trajectory as seen from the Earth—the curvature of the line is due to the parallax effect. The small empty circles represent the size and positions of the source star at both epochs. Also marked are the positions of the planet (small dots on the right) and its host star (big dots on the left)—the displacement of the planet due to its orbital motion over 11 days between the perturbations is clearly visible. The origin is at the center of mass of the planetary system. The horizontal axis is parallel with the star-planet axis at the time t_0.

Figure 4. Cumulative χ^2 distributions as a function of a data point number for three microlensing models. The vertical bands mark the time of the major and minor planetary anomaly. We see that the minor anomaly cannot be well fitted without the inclusion of the lens orbital motion. The two anomalies appeared in the light curve closer in time than could be fit with a static binary model. Since the first anomaly is extremely well covered with observations, the second anomaly does not fit the best possible static model.

ratio of the number density of rays on the source surface to the density on the image plane. This numerical technique requires heavy computation and thus we limit finite magnification computation based on the ray-shooting method to the region very close to caustics. In the adjacent region, we use a hexadecapole approximation, with which finite magnification computation can be faster by several orders of magnitude (Gould 2008; Pejcha & Heyrovský 2009). We solve the lens equation by using the complex polynomial method described in Skowron & Gould (2012).
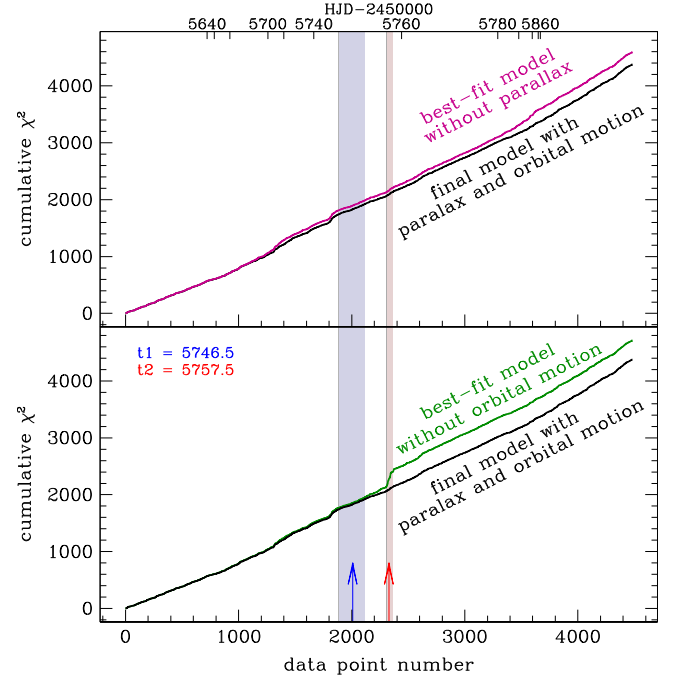
In computing finite-source magnifications, we incorporate the limb-darkening variation of the stellar surface brightness. The surface brightness profile is modeled as $S_\lambda \propto 1 - c_\lambda \cdot (1 - \cos\phi) - d_\lambda \cdot (1 - \sqrt{\cos\phi})$, where c_λ and d_λ are the limb-darkening coefficients of the wavelength band λ, and ϕ is the angle between the normal to the stellar surface and the line of sight toward the center of the star. Based on the stellar type (see Section 5), we adopt the coefficients using Table 32 (square-root law) of Claret (2000) for $v_t = 2$, solar metallicity, $T_{eff} = 5000$ K, and $\log g = 3.5$:

$$c_{I-band}, d_{I-band} = 0.2288, 0.4769, \tag{5}$$

$$c_{MOA-R}, d_{MOA-R} = 0.2706, 0.4578, \tag{6}$$

$$c_{V-band}, d_{V-band} = 0.5337, 0.2993. \tag{7}$$

Here the values for the non-standard MOA-R filter are taken as linear combination of the R-band and I-band coefficients with 30% and 70% weights.

4. RESULTS

4.1. Best-fit Solution

In Table 1, we present the best-fit solutions along with their χ^2 values. In order to provide information about the blended light (i.e., the light that was not magnified during the event), we also present the source, F_S, and baseline, F_{base}, fluxes estimated from the OGLE photometry. We note that the uncertainty of each parameter is estimated based on the distribution in the MCMC chain obtained from modeling.

It is found that the perturbation was produced by a planetary companion with a planet/star mass ratio $q \sim 3.9 \times 10^{-3}$ located close to the Einstein ring of its host star (i.e., $s \sim 1.0$). In the upper panel of Figure 3, we present the locations of the lens components, the caustic, and the source trajectory for the best-fit solution. Since the planet is close to the Einstein ring, the resulting caustic forms a single closed curve with six cusps. The major (at $HJD' = 5746.5$) and minor (at $HJD' = 5757.5$) perturbations in the lensing light curve were produced by the approach of the source star close to the strong and weak cusps of the caustic, respectively.

We find that the event suffers from the ecliptic degeneracy. In Figure 3, we compare the lens-system geometry of the two degenerate solutions with $u_0 < 0$ and $u_0 > 0$. We note that the source trajectories of the two degenerate solutions are almost symmetric with respect to the star-planet axis. The χ^2 difference between the two degenerate models is merely 5.7—with $u_0 > 0$ solution slightly preferred over the $u_0 < 0$ solution. We further discuss this degeneracy in Section 5.2.
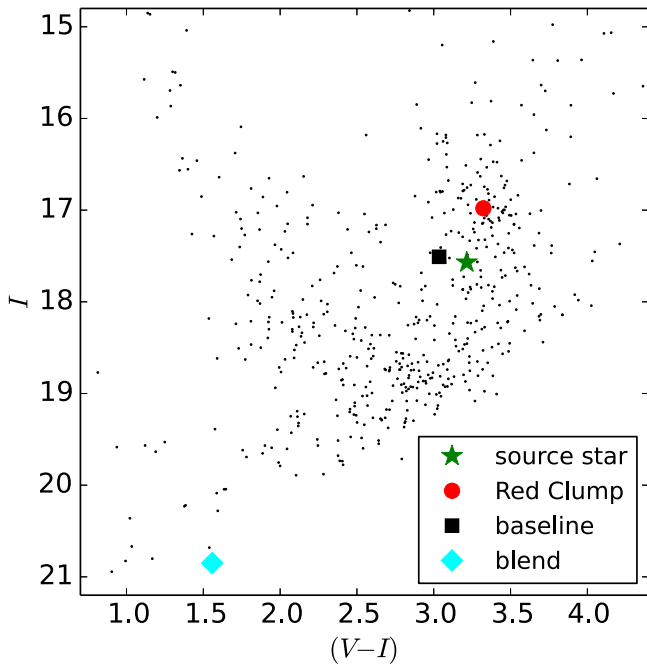
Figure 5. Location of the source star in the OGLE color–magnitude diagram for stars in the $1\!.\!5 \times 1\!.\!5$ field centered on the lensing event. Also shown is the centroid of the red clump giant stars that is used to calibrate the brightness and color of the source star. Light seen before and after the event (baseline level) was separated into the "source" and the "blend" light (or the portion of light that was magnified and the portion that was not magnified during the course of the event, respectively).

Higher-order effects are important for the event. We find that the model considering the parallax effect improves the fit with $\Delta\chi^2 = 230.9$ for $u_0 > 0$ and 127.8 for $u_0 < 0$ compared to the standard model. The model considering the lens orbital motion (but without parallax) improves the fit even more, with $\Delta\chi^2 = 349.1$ compared to the standard model. Considering both the parallax and orbital effects yields a light curve model that fits the data significantly better, with $\Delta\chi^2 = 559.4$ for $u_0 > 0$ and 565.1 for $u_0 < 0$ relative to the standard model.

The importance of the lens orbital motion can be seen in Figure 4, which shows the cumulative χ^2 distribution for the full (final) model, and compares it to the models without the parallax effect (upper panel) and without the lens orbital motion (lower panel) taken into account. It is found that the signal of the orbital effect is mainly seen from the part of the light curve at around $\mathrm{HJD'} \sim 5757.5$, which corresponds to the time of the minor anomaly. The second anomaly happened sooner than predicted by the static binary model. Without the observations at this time, we would have lacked the information on the evolution of the the caustic shape during the time between the anomalies. The minor anomaly was densely covered by follow-up data, especially the SAAO data, but the coverage by the survey data is sparse. As a result, the orbital parameters could not be well constrained by the survey data alone.

4.2. Angular Einstein Radius

Detection of the microlens parallax enables the measurement of the mass and distance to the planetary system. The Einstein radius, which is the second component required by Equations (2) and (3), is estimated by $\theta_E = \theta_*/\rho$, where the angular

source radius θ_* is obtained from the color and brightness information, and the normalized source radius ρ is measured from the microlensing light curve fitting to the planetary perturbation.

4.2.1. Intrinsic Color and Extinction-corrected Brightness of the Source Star

To determine the angular source radius, we first locate the source star on the color–magnitude diagram for stars in the field, and then calibrate its dereddened color and brightness by using the centroid of the red clump giants as a reference under the assumption that the source and red clump giants experience the same amount of extinction and reddening (Yoo et al. 2004).

In Figure 5 we present the location of the source star in the color–magnitude diagram. Using the method of Nataf et al. (2010) finding the centroid of the red clump in the $1\!.\!5 \times 1\!.\!5$ region of the sky around the source star, we estimate that the source star (with $V = 20.77$ and $I = 17.57$) is 0.12 mag bluer and 0.59 mag fainter than the typical red clump giant, and hence, is most likely also a K-type giant star located in the Galactic bulge. Based on the intrinsic color of the red clump giant stars $(V - I)_{\mathrm{RC},0} = 1.06$ (Bensby et al. 2011), we estimate the dereddened color of the source star to be $(V - I)_{\mathrm{S},0} = 0.94$.

With the observed $((V - I)_{\mathrm{RC}} = 3.32)$ and intrinsic colors of the red clump stars, we estimate the total reddening toward the Galactic Bulge:

$$E(V - I) = (V - I)_{\mathrm{RC}} - (V - I)_{\mathrm{RC},0}$$
$$= 3.32 - 1.06 = 2.26. \qquad (8)$$

From Nataf et al. (2013) the mean distance to the Galactic bulge stars in the direction of the event is 7.8 kpc and the intrinsic brightness of the red clump stars is $M_{I,\mathrm{RC},0} = -0.11$. With the measured observed brightness $I_{\mathrm{RC}} = 16.98$, we estimate the extinction to the bulge to be $A_I = 2.63$. This is consistent with the estimated reddening of 2.26, as the slope of the reddening vector $(\partial A_I/\partial E(V - I))$ is typically ~ 1.2, and in most cases is between 1.0 and 1.4 for the Galactic bulge sight lines (Nataf et al. 2013, Figure 7). The extinction in the V band is calculated as $A_V = A_I + E(V - I) = 4.89$. Then, the extinction-corrected magnitudes of the source star are computed as

$$V_{\mathrm{S},0} = V_\mathrm{S} - A_V = 20.77 - 4.89 = 15.88, \qquad (9)$$

$$I_{\mathrm{S},0} = I_\mathrm{S} - A_I = 17.57 - 2.63 = 14.94. \qquad (10)$$

4.2.2. Uncertainties of the Source Color Estimation

Although uncertainties of the observed color and brightness of the source stars are typically low (in this case 0.01 mag), the uncertainty in the centroiding of the red clump and the differential reddening in the field means that the true intrinsic colors of the microlensing sources are typically known with lower accuracy. Bensby et al. (2013, Section 3.2) compare the colors of source stars of the 55 microlensing events determined with both spectroscopic and microlensing techniques. Their Figure 5 shows that the disagreement between the two estimations is typically 0.07 mag for the blue star sample and 0.08 mag for all stars. There is no physical reason for the measurement of the color offset from the red clump stars to be

Table 2
Physical Lens Parameters

Quantity	$u_0 > 0$ Solution	$u_0 < 0$ Solution
θ_E (mas)	0.419 ± 0.040	0.423 ± 0.040
μ_{geo} (mas yr^{-1})	2.85 ± 0.29	2.89 ± 0.29
$\mu_{hel,N}$ (mas yr^{-1})	2.72 ± 0.30	2.73 ± 0.32
$\mu_{hel,E}$ (mas yr^{-1})	$1.06^{+0.29}_{-0.18}$	$1.39^{+0.19}_{-0.16}$
M_p (M_J)	$0.88^{+0.27}_{-0.18}$	$0.56^{+0.25}_{-0.13}$
M_h ($M_\odot$)	$0.211^{+0.068}_{-0.045}$	$0.136^{+0.061}_{-0.031}$
D_L (kpc)	$4.38^{+0.51}_{-0.45}$	$3.49^{+0.71}_{-0.49}$
$a_\perp$ (AU)	$1.89^{+0.25}_{-0.20}$	$1.51^{+0.31}_{-0.20}$
$(KE/PE)_\perp$	0.387 ± 0.075	0.112 ± 0.060

Note. The parameters calculated for parallax+orbital model. θ_E, angular Einstein radius; μ_{geo} and μ_{hel}, relative lens-source proper motion in the geocentric and heliocentric reference frames, respectively; M_p, mass of the planet; M_h, mass of the host star; D_L, distance to the lens; $a_\perp$, projected star-planet; and $(KE/PE)_\perp$, the ratio of the transverse kinetic to potential energy.

less accurate for red stars than for blue stars. Hence, the authors point to, clearly but not perfectly, the color–T_{eff} relations as the source of the increased scatter for red stars (with $T_{eff} < 5500$ K, see Bensby et al. 2013, Figure 7). The observed 0.07 mag scatter between the spectroscopic and microlensing color estimates also includes the uncertainties in T_{eff}, which are of the order of 100 K and would generate ~0.034 mag uncertainty in color (compared with Table 5 and Figure 7 of Bensby et al. 2013). By subtracting this source of scatter in quadrature from the observed scatter, we obtain 0.061 mag, which still contains some unknown uncertainty of the stellar models themselves.

The sample of events analyzed by Bensby et al. (2013) also contains some problematic events of two types. One type is events where the coverage of the light curve in the multiple photometric bands was not sufficient to accurately determine observed color, while the other type is events in the fields with poorly defined red clumps. This allows us to argue that for well observed microlensing events in fields with a well defined red clump, the typical error in the microlensing color estimation is on the order of 0.05 mag.

One could worry that the assumption of a typical error of the intrinsic color estimation does not take into account the influence of the differential reddening, which in fact, varies from field to field. Figure 6 of Bensby et al. (2013) addresses this issue, showing that there is no evidence of strong correlation between the differential reddening in the fields of 55 events (as measured by Nataf et al. 2013) and errors in their color estimations. This actually could be understood by realizing that the dominating source of scatter in the observed colors of red clump stars comes from the gradient of the reddening across the field. This gradient, however, has no effect on the position of the red clump stars centroid.

As an example, we took samples of stars from four circles centered on our event with the diameters of 1.5′, 2′, 3′, and 4′, respectively, and used them to measure the centroid of the red clump. All four measurements are within 0.02 mag of each other, even though the measure of the differential reddening (as defined by Nataf et al. 2013) is between 0.16 and 0.24 in these circles.

It is also worth noting that any error in the relative position of the source star from the centroid of the red clump that could come from the differential reddening would only partially contribute to the final estimation of the angular size of the star. As we will see in the following section, the calibration of the angular radius of the star contains two terms with opposite signs: $\sim 0.5(V - I)_0 - 0.2I_0$ (Equation (11)). More dust in front of the star influences both estimations of $(V - I)_0$ and I_0 in the same direction, and since $A_I \approx 1.2\, E(V - I)$, the overall error that comes from the wrong estimation of the reddening is reduced by 50% ($1.2 \times 0.2/0.5 = 0.5$).

The OGLE-2011-BLG-0265 event is located 1.°5 from the Galactic plane in the region strongly obscured by the interstellar dust ($E(V - I) = 2.26$) and affected by the differential reddening. Following Nataf et al. (2013), we calculate the measure of the differential reddening ($\sigma_{E(V-I)}$) in the 1.′5 × 1.′5 patch of the sky around the event. The observed $V - I$ colors of the red clump stars show 0.20 mag dispersion, which leads to the estimation of $\sigma_{E(V-I)} = 0.16$ mag. However, having the evidence for at most minor influence of the differential reddening on the final estimation of the color, and knowing that only half of the error (due to reddening) enters the final result, we only slightly increase our uncertainty of the color from 0.05 to 0.06 mag due to the heavily reddened field.

We expect the error in the estimation of I_0 to be slightly higher than the assumed error for $(V - I)_0$. In order to measure the observed brightness of the red clump, the luminosity function of the red giant branch has to be fitted simultaneously with the luminosity function of the red clump giants. Based on the reproducibility of the red clump centroiding under various assumptions regarding the red giant branch luminosity function, we conservatively assume a 0.1 mag error in the estimation of I_0 of the source star.

4.2.3. Angular Size from the Surface Brightness Relations

Knowing the dereddened color of the star and the extinction-corrected brightness enables the use of the surface brightness relation to find the angular radius (θ_*). We note that in microlensing we typically measure $(V - I)_0$ color, hence, ideally we would like to use a calibration based on this quantity. By including the additional transformation process from $(V - I)_0$ to $(V - K)_0$, the uncertainty of the estimated color increases by a factor 1.5–2.5 (e.g., $\partial(V - K)/\partial(V - I) \approx 2.5$ for stars with $(V - I) < 1.3$ Bessell & Brett 1988). Kervella & Fouqué (2008) provide such a relation calibrated with dwarfs and subgiant stars; we write:

$$\log\theta_* = 3.1982 - 0.2I_0 + 0.4895(V - I)_0 - 0.0657(V - I)_0^2, \tag{11}$$

where the angular radius is given in μas and the scatter of the relation is 0.0238. The relation in $(V - K)$ for the same types of stars based on Kervella et al. (2004) is

$$\log\theta_* = 3.2165 - 0.2V_0 + 0.2753(V - K)_0 \tag{12}$$

and the quadratic relation for the wider range of stars was given by Di Benedetto (2005):

$$\log\theta_* = 3.2120 - 0.2V_0 + 0.2968(V - K)_0 - 0.0088(V - K)_0^2. \tag{13}$$

Kervella & Fouqué ([2008](#)) believe that the scatter around the provided relation is dominated by the intrinsic scatter rather than measurement errors. This yields the relative uncertainty of the angular radius at 5.5%. Calibrations based on an infrared color have much smaller intrinsic scatter, so careful removal of the scatter due to measurement error is required. Kervella et al. ([2004](#)) estimate that the intrisic scatter around the provided relation is 1%, whereas Di Benedetto ([2005](#)) estimates 1.8% and argues that the accuracy of the star sizes obtained from the infrared-based surface brightness relations is <2%, but higher than the 1% estimated by Kervella et al. ([2004](#)).

We note that despite having much smaller scatter, the relations with $(V - K)_0$ (transformed from $(V - I)_0$) yield higher uncertainty of the angular radius than the relation originally calibrated in $(V - I)_0$, unless the accuracy of the $(V - I)_0$ estimation is $\lesssim 0.05$ or $(V - I)_0 > 1.3$, where the slope of $(V - K)$ versus $(V - I)$ is more shallow. Hence, we use the Kervella & Fouqué ([2008](#)) relation in the OGLE-2011-BLG-0265 case, which leads to the final estimation of the angular source radius

$$\theta_* = 4.09 \pm 0.41 \ \mu\text{as}. \tag{14}$$

Combining the physical and the normalized source radius yields the Einstein radius of $\theta_E = \theta_*/\rho = 0.42 \pm 0.04$ mas (for both $u_0 > 0$ and $u_0 < 0$ solutions of the parallax+orbit model).

4.3. Physical Parameters

With the measured Einstein radius and the lens parallax, we are able to estimate the physical quantities of the lens system (Table [2](#)). For the best-fit solution ($u_0 > 0$, parallax+orbit model), the lens mass and distance to the lens are $M = 0.22 \pm 0.06 \ M_\odot$ and $D_L = 4.4 \pm 0.5$ kpc, respectively. The mass of the planet is $M_p = 0.9 \pm 0.3 \ M_J$. The projected separation between the host star and the planet is $a_\perp = 1.9 \pm 0.2$ AU and thus the planet is located well beyond the snow line of the host star.

For the marginally disfavored $u_0 < 0$ solution, the resulting physical parameters of the lens system are somewhat different —as expected, they are mainly caused by the difference in the north component of the parallax vector (i.e., $\pi_{E,N}$). See Table [1](#). In this case, the lens mass and distance are $M = 0.14 \pm 0.06 \ M_\odot$ and $D_L = 3.5 \pm 0.7$ kpc, respectively, and the mass of the planet is $M_p = 0.6 \pm 0.3 \ M_J$.

Hence, the system belongs to a little-known population of planetary systems, where a Jupiter-mass planet orbits an M dwarf beyond its snow line.

5. DISCUSSION

5.1. Degeneracy of the Microlensing Models

While the planetary nature of the perturbation in the OGLE-2011-BLG-0265 light curve is obvious, the event suffers from the orbiting binary ecliptic degeneracy (Skowron et al. [2011](#), see Appendix 3). The two solutions, $u_0 < 0$ and $u_0 > 0$, have nearly identical mass ratio $q = 3.9 \times 10^{-3}$, normalized separation $s = 1.04$, and Einstein radius $\theta_E = 0.42$ mas, and hence planet–host angular separation $\theta_\perp = 0.44$ mas. They differ in the microlens parallax, especially in the north component $\pi_{E,N} = 0.24$ ($u_0 > 0$) versus $\pi_{E,N} = 0.38$ ($u_0 < 0$), and also in $d\alpha/dt$, which is often strongly correlated

with $\pi_{E,N}$ (Batista et al. [2011](#); Skowron et al. [2011](#)). This difference is important because it leads to a different mass and distance of the host $(M_*/M_\odot, D_L/\text{kpc}) = (0.22, 4.4)$ versus $(0.14, 3.5)$ for the $u_0 > 0$ and $u_0 < 0$ solutions, respectively.

The $u_0 > 0$ solution is favored by $\Delta\chi^2 = 5.7$ corresponding to a (frequentist) likelihood ratio of $\exp(5.7/2) = 17$. This would be compelling evidence if treated at face value. However, it is known that the photometry of microlensing events occasionally suffers from low-level systematic trends at $\Delta\chi^2 \sim$ few level.

As an additional way to resolve the degeneracy, we check the ratio of the projected kinetic to potential energy (Dong et al. [2009](#)) estimated by

$$\beta = \left(\frac{\text{KE}}{\text{PE}}\right)_\perp = \frac{v_\perp^2 r_\perp}{2 \ GM_{\text{tot}}} = \frac{\kappa M_\odot \text{yr}^2}{8\pi^2} \frac{\pi_E s^3 \gamma^2}{\theta_E (\pi_E + \pi_S/\theta_E)^3}, \tag{15}$$

where $\gamma^2 = (ds/dt/s)^2 + (d\alpha/dt)^2$. For typical viewing angles, one expects $\beta \sim \mathcal{O}(0.4)$, as is the case for the $u_0 > 0$ solution. On the other hand, the lower value $\beta \sim 0.11$ (as in the $u_0 < 0$ solution) implies either that the planet is seen projected along the line of sight at the viewing angle $\psi \sim 2\beta \sim 0.22$ (corresponding to the semimajor axis $a \sim a_\perp/(2\beta) \sim 4.5a_\perp$), or that we have just seen the planet when majority of its motion is directly toward (or away from) us. Of course, the prior probability of the first configuration for a point randomly distributed on a sphere is just $2\beta^2 \sim 0.025$ and the probability for the second is similar.

However, while it is certainly true that the prior probability for any given planet's position is uniform over a sphere, this is not the case for planets found by microlensing, which are preferentially detected within a factor of ∼1.5 of the Einstein radius (Gould & Loeb [1992](#); Gould et al. [2010](#)). First, since the planet actually lies very near the Einstein radius, it would have been detected in almost any angular orientation α, so that the actual probability is more like β than β^2 (i.e., about 0.11). In addition, since giant planets around the M dwarfs are a new class of planets, we do not know their distribution. It could be that the great majority of such planets lie at $a \sim 20$ AU. Then, whenever these were found in planet–host microlensing events, they would have a very low value β. On the other hand, whenever we detect them at typical viewing angles, they will be considered as "free-floating planets" (Sumi et al. [2011](#)). Hence, the measurement of a low β value is not a strong statistical argument against the $u_0 < 0$ solution, which still remains as a viable option.

In summary, although both light curve and energy considerations point to the $u_0 > 0$ solution, it is difficult to confidently resolve the degeneracy between the two possible models based on the currently available data. Fortunately, the difference in the physical parameters estimated from the two degenerate solutions is not big enough to affect the conclusion that the lens belongs to a new class of giant planets around low-mass stars.

5.2. Prospects for Follow-up Observations

It will eventually be possible to confidently resolve the current degeneracy issue on the models of OGLE-2011-BLG-0265 when the Giant Magellan Telescope comes on line in about 10 yr. At that time, the source and lens will be separated

by about 40 mas, or roughly three FWHM in the J-band. There are three observables that can then be used to distinguish the two solutions. First, the $u_0 < 0$ solution predicts a fainter lens because it has a lower mass. Second, it predicts slightly higher heliocentric proper motion (mainly in the east sky direction). Third, it predicts a different angle of the proper motion.

Each of these measurements has some potential problems. The prediction of the lens flux is influenced not only by the mass and the distance, but also by the extinction to the lens. There is a substantial error in θ_E that impacts the brightness in the same direction as the mass and distance. That is, if θ_E is higher than we have estimated, then the distance is closer (so the lens is brighter) and the mass is greater (so the lens is brighter again). Fortunately, the detection of the lens will itself enable us to measure the proper motion μ_{hel} and therefore also the Einstein radius (see below). Also, with a bigger telescope, it will be possible to better estimate θ_E by detailed characterization of the source star, thus, a more accurate estimation of the θ_* in Equation (14).

As can be seen from Table 2, the predictions for heliocentric proper motion differ by only 1σ. This is the same problem as just mentioned: the proper motion prediction contains the significant error of θ_E.

By contrast, the angle of heliocentric proper motion, ϕ_μ, does not depend on θ_E. In terms of observables,

$$\boldsymbol{\mu}_{hel} = \frac{\theta_E}{t_E}\frac{\boldsymbol{\pi}_E}{\pi_E} + \frac{\boldsymbol{v}_{\oplus,\perp}}{AU}\pi_{rel} = \theta_E\left(\frac{1}{t_E}\frac{\boldsymbol{\pi}_E}{\pi_E} + \frac{\boldsymbol{v}_{\oplus,\perp}}{AU}\pi_E\right), \quad (16)$$

where $\boldsymbol{v}_{\oplus,\perp}$ is the motion of Earth projected on the sky at the fiducial time of the event $(v_{\oplus,N}, v_{\oplus,E}) = (-0.42, 5.45)$ AU yr^{-1}. This means that the position angle (north through east) is

$$\phi_\mu = \mathrm{atan}\frac{\pi_{E,E} + \pi_E^2 v_{\oplus,E} t_E/AU}{\pi_{E,N} + \pi_E^2 v_{\oplus,N} t_E/AU}, \quad (17)$$

which is indeed independent of θ_E. We find $\phi_\mu = 20.8^{+5.3}_{-2.7}$ deg for $u_0 > 0$ and $\phi_\mu = 26.4^{+2.0}_{-1.2}$ deg for $u_0 < 0$. Thus if the actual measurement is $\phi_\mu = 21°$, it will strongly exclude (4σ) the $u_0 < 0$ solution, but if it is $\phi_\mu = 26°$ then it will only marginally favor (1σ) the $u_0 < 0$ solution.

Nevertheless, with these three pieces of information, there is a good chance that the ensemble of measurements will favor one solution or the other.

6. CONCLUSIONS

We reported the discovery of a planet detected by analyzing the light curve of the microlensing event OGLE-2011-BLG-0265. It is found that the lens is composed of a giant planet orbiting a M-type dwarf host. Unfortunately, the microlensing modeling yields two degenerate solutions, which increases our uncertainties in mass of and distance to this planetary system, and cannot be distinguished with the currently available data. The planet–host mass ratio is, however, very well measured at 0.0039.

The slightly preferred solution yields a Jupiter-mass planet orbiting a $0.22\,M_\odot$ dwarf. The second solution yields a 0.6 Jupiter-mass planet orbiting a $0.14\,M_\odot$ dwarf. There are good prospects for lifting the degeneracy of the solutions with future additional follow-up observations. In either case, the OGLE-2011-BLG-0265 event demonstrates the uniqueness of the microlensing method in detecting planets around low-mass stars.

REFERENCES

Alard, C., & Lupton, R. H. 1998, ApJ, 503, 325
Albrow, M. D., Beaulieu, J.-P., Caldwell, J. A. R., et al. 2000, ApJ, 534, 894
Albrow, M. D., Horne, K., Bramich, D. M., et al. 2009, MNRAS, 397, 2099
Batista, V., Gould, A., Dieters, S., et al. 2011, A&A, 529, A102
Beaulieu, J.-P., Bennett, D. P., Fouqué, P., et al. 2006, Natur, 439, 437
Bennett, D. P., & Rhie, S. H. 1996, ApJ, 472, 660
Bennett, D. P., Bond, I. A., Udalski, A., et al. 2008, ApJ, 684, 663
Bennett, D. P., Rhie, S. H., Nikolaev, S., et al. 2010, ApJ, 713, 837
Bensby, T., Adén, D., Meléndez, J., et al. 2011, A&A, 533, AA134
Bensby, T., Yee, J. C., Feltzing, S., et al. 2013, A&A, 549A, 147
Bessell, M. S., & Brett, J. M. 1988, PASP, 100, 1134
Bond, I. A., Abe, F., Dodd, R. J., et al. 2001, MNRAS, 327, 868
Bonfils, X., Gillon, M., Forveille, T., et al. 2011, A&A, 528, 111
Boss, A. P. 2006, ApJ, 643, 501
Bramich, D. M. 2008, MNRAS, 386, L77
Cassan, A., Kubas, D., Beaulieu, J.-P., et al. 2012, Natur, 481, 167

Charbonneau, D., Berta, Z. K., & Irwin, J. 2009, Natur, 462, 891
Claret, A. 2000, A&A, 363, 1081
Delfosse, X., Forveille, T., Mayor, M., et al. 1998, A&A, 338, L67
Di Benedetto, G. P. 2005, MNRAS, 357, 174
Dominik, M., Jørgensen, U. G., Rattenbury, N. J., et al. 2010, AN, 331, 671
Dong, S., DePoy, D. L., Gaudi, B. S., et al. 2006, ApJ, 642, 842
Dong, S., Gould, A., Udalski, A., et al. 2009, ApJ, 695, 970
Gaudi, B. S., Bennett, D. P., Udalski, A., et al. 2008, Sci, 319, 927
Gould, A. 1992, ApJ, 392, 442
Gould, A., & Loeb, A. 1992, ApJ, 396, 104
Gould, A. 2008, ApJ, 681, 1593
Gould, A., Udalski, A., An, D., et al. 2006, ApJL, 644, L37
Gould, A., Dong, S., Gaudi, B. S., et al. 2010, ApJ, 720, 1073
Ida, S., & Lin, D. N. C. 2005, ApJ, 626, 1045
Kains, N., Street, R. A., Choi, J.-Y., et al. 2013, A&A, 552, A70
Kayser, R., Refsdal, S., & Stabell, R. 1986, A&A, 166, 36
Kervella, P., Thévenin, F., Di Folco, E., & Ségransan, D. 2004, A&A, 426, 297
Kervella, P., & Fouqué, P. 2008, A&A, 491, 855
Kubas, D., Beaulieu, J.-P., Bennett, D. P., et al. 2012, A&A, 540, 78
Laughlin, G., Bodenheimer, P., & Adams, F. C. 2004, ApJL, 612, L73
Mao, S., & Paczyński, B. 1991, ApJL, 374, L37
Marcy, G. W., Butler, R. P., Vogt, S. S., Fischer, D., & Lissauer, J. J. 1998, ApJL, 505, L147
Montet, B. T., Crepp, J. R., Johnson, J. A., Howard, A. W., & Marcy, G. W. 2014, ApJ, 781, 28

Nataf, D. M., Udalski, A., Gould, A., Fouqué, P., & Stanek, K. Z. 2010, ApJL, 721, L28
Nataf, D. M., Gould, A., Fouqué, P., et al. 2013, ApJ, 769, 88
Paczyński, B. 1986, ApJ, 304, 1
Park, H., Udalski, A., Han, C., et al. 2013, ApJ, 778, 134
Pejcha, O., & Heyrovský, D. 2009, ApJ, 690, 1772
Penny, M. T., Mao, S., & Kerins, E. 2011, MNRAS, 412, 607
Poleski, R., Udalski, A., Dong, S., et al. 2014, ApJ, 782, 47
Schechter, P. L., Mateo, M., & Saha, A. 1993, PASP, 105, 1342
Schneider, P., & Weiss, A. 1986, A&A, 164, 237
Shin, I.-G., Udalski, A., Han, C., et al. 2011, ApJ, 735, 85
Shvartzvald, Y., & Maoz, D. 2012, MNRAS, 419, 3631
Shvartzvald, Y., Maoz, D., Kaspi, S., et al. 2014, MNRAS, 439, 604
Skowron, J., Udalski, A., Gould, A., et al. 2011, ApJ, 738, 87
Skowron, J., & Gould, A. 2012, arXiv:1203.1034
Sumi, T., Bennett, D. P., Bond, I. A., et al. 2010, ApJ, 710, 1641
Sumi, T., Kamiya, K., Bennett, D. P., et al. 2011, Natur, 473, 349
Street, R. A., Choi, J.-Y., Tsapras, Y., et al. 2013, ApJ, 763, 67
Tsapras, Y., Horne, K., Kane, S., & Carson, R. 2003, MNRAS, 343, 1131
Tsapras, Y., Street, R., Horne, K., et al. 2009, AN, 330, 4
Tsapras, Y., Choi, J.-Y., Street, R. A., et al. 2014, ApJ, 782, 48
Udalski, A. 2003, AcA, 53, 291
Udalski, A., Jaroszyński, M., Paczyński, A., et al. 2005, ApJL, 628, L109
Wambsganss, J. 1997, MNRAS, 284, 172
Yoo, J., DePoy, D. L., Gal-Yam, A., et al. 2004, ApJ, 603, 139